Supplementary Information for:

Characterizing Microscopic Calcification Deposits on Acrylic Intraocular Lenses

Cassandra L. Ward[1]*, S. Sameera Perera[1], Zhi Mei[1], Bing X. Ross[2], Manisha De Alwis Goonatilleke[3], Mahdi Ayoubi[3], Yao Xiao[4], Andrew P. Ault[4], Judy A. Westrick[1], Thomas H. Linz[5], Xihui Lin[2]

1. Lumigen Instrument Center, Wayne State University, Detroit, Michigan
2. Kresge Eye Institute/Department of Ophthalmology, Visual and Anatomical Sciences, Wayne State University School of Medicine, Detroit, Michigan
3. Thermo Fisher Scientific, Hillsboro, Oregon.
4. Department of Chemistry, University of Michigan, Ann Arbor, Michigan
5. Department of Chemistry, Wayne State University, Detroit, Michigan

Supplementary Information Contents:

Lenses 2–5 Images and PXRD:

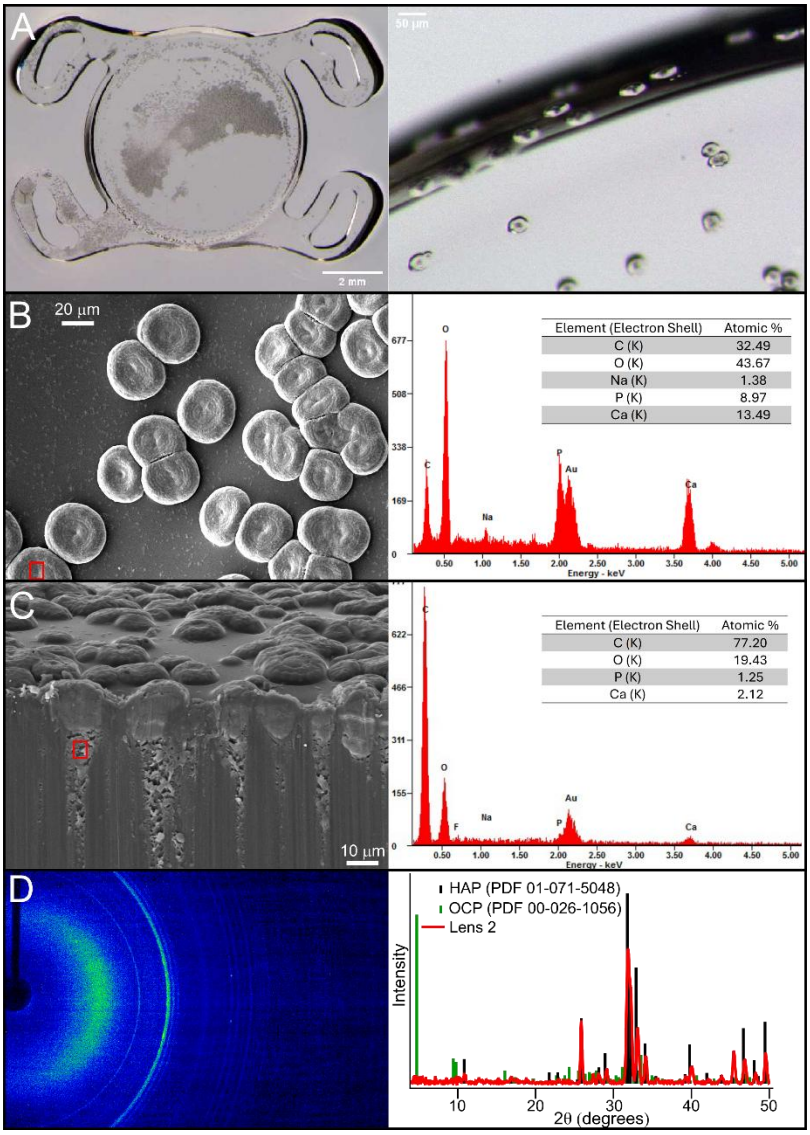

Figure S1. Lens 2 **(A)** micrographs of the whole IOL (left) and zoomed region on the optic edge (right), **(B)** top-down SEM image (left) and EDS (right) of a crystal (red box), **(C)** cross-sectional SEM image (left) and EDS (right) of a pore (red box), and **(D)** 2D-XRD data of the crystals (left) and the integrated data (right).

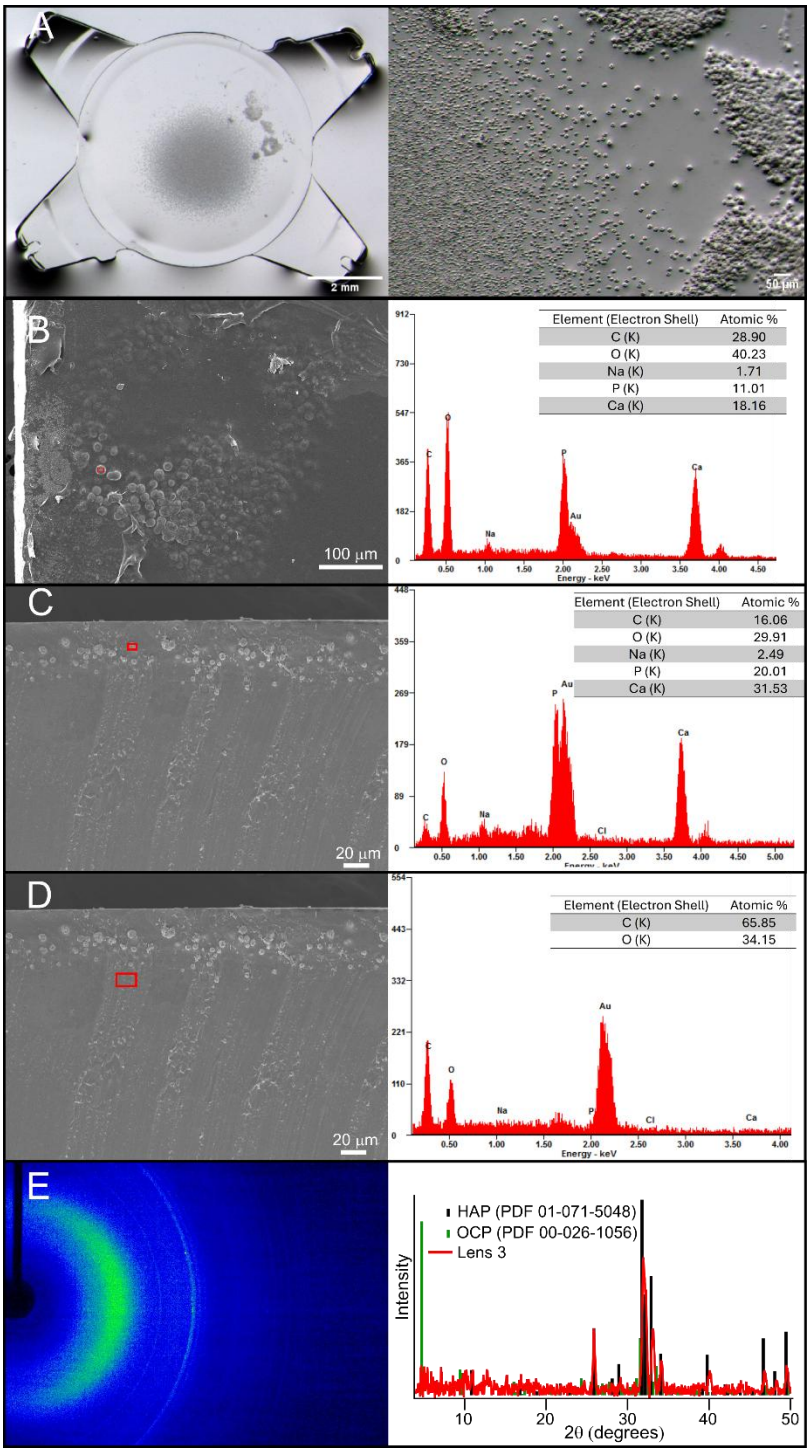

Figure S2. Lens 3 **(A)** micrographs of the whole IOL (left) and zoomed region on the optic center (right), **(B)** top-down SEM image (left) and EDS (right) of a crystal (red box), **(C)** cross-sectional SEM image (left) and EDS (right) of a crystal (red box), **(D)** cross-sectional SEM image (left) and EDS (right) of a pore (red box) and **(E)** 2D-XRD data of the crystals (left) and the integrated data (right).

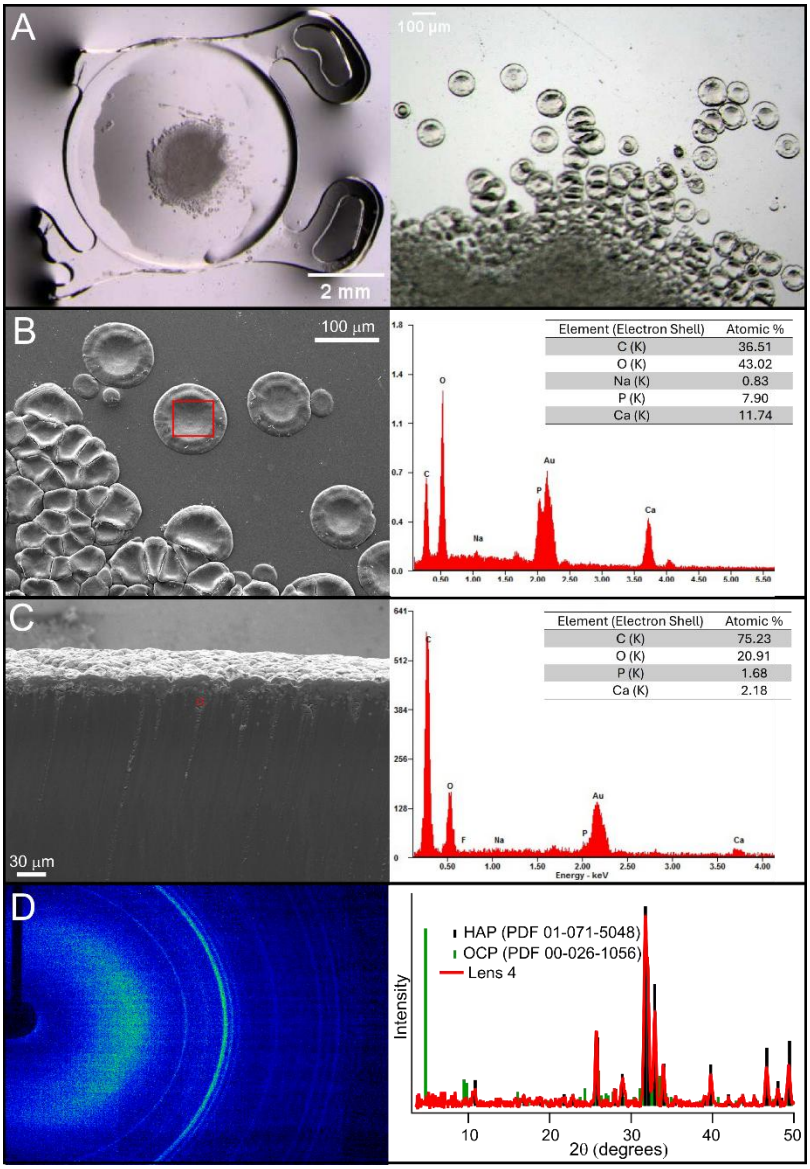

Figure S3. Lens 4 **(A)** micrographs of the whole IOL (left) and zoomed region on the optic center (right), **(B)** top-down SEM image (left) and EDS (right) of a crystal (red box), **(C)** cross-sectional SEM image (left) and EDS (right) of crystals in a channel (red box), and **(D)** 2D-XRD data of the crystals (left) and the integrated data (right).

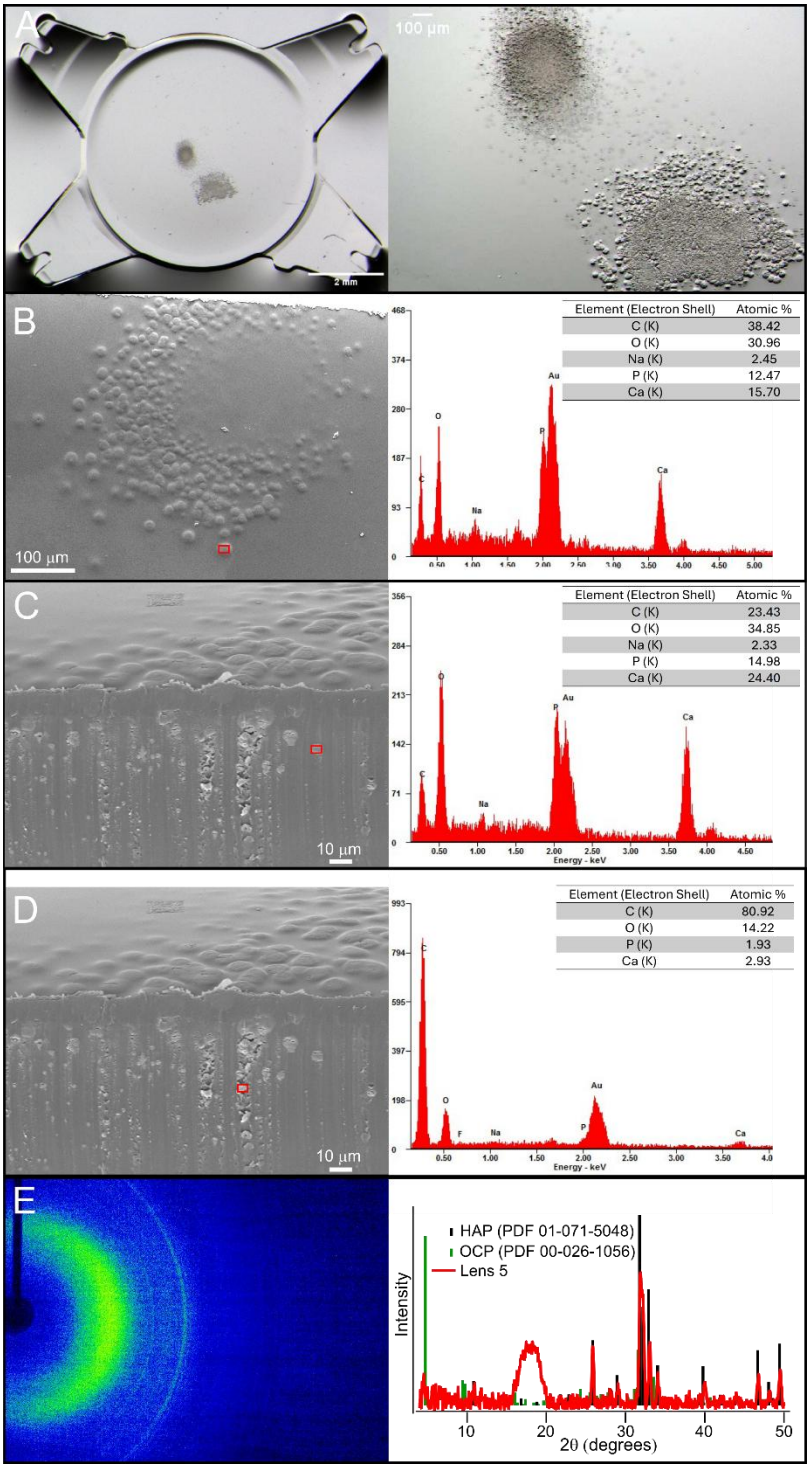

Figure S4. Lens 5 **(A)** micrographs of the whole IOL (left) and zoomed region on the optic center (right), **(B)** top-down SEM image (left) and EDS (right) of a crystal (red box), **(C)** cross-sectional SEM image (left) and EDS (right) of a crystal (red box), **(D)** cross-sectional SEM image (left) and EDS (right) of a pore (red box) and **(E)** 2D-XRD data of the crystals (left) and the integrated data (right).

Ca/P Ratio Using XPS:

The Ca/P ratio of the crystals on Lens 1 was calculated using the high-resolution (HR)-XPS scans to integrate the area under the Ca 2P peaks and the P 2P peaks. HR-XPS scans were measured from multiple locations on Lens 1 using the flat areas of the optic edge and haptic regions.[1] A survey spectrum recorded at IOL location 1 and the peak fits for high-resolution Ca 2p and P 2p spectra acquired for analysis locations 1–5 are shown in **Figure S5**. The average of the Ca/P ratio was 1.53 ± 0.09, which is consistent with the EDS results (Table S1).

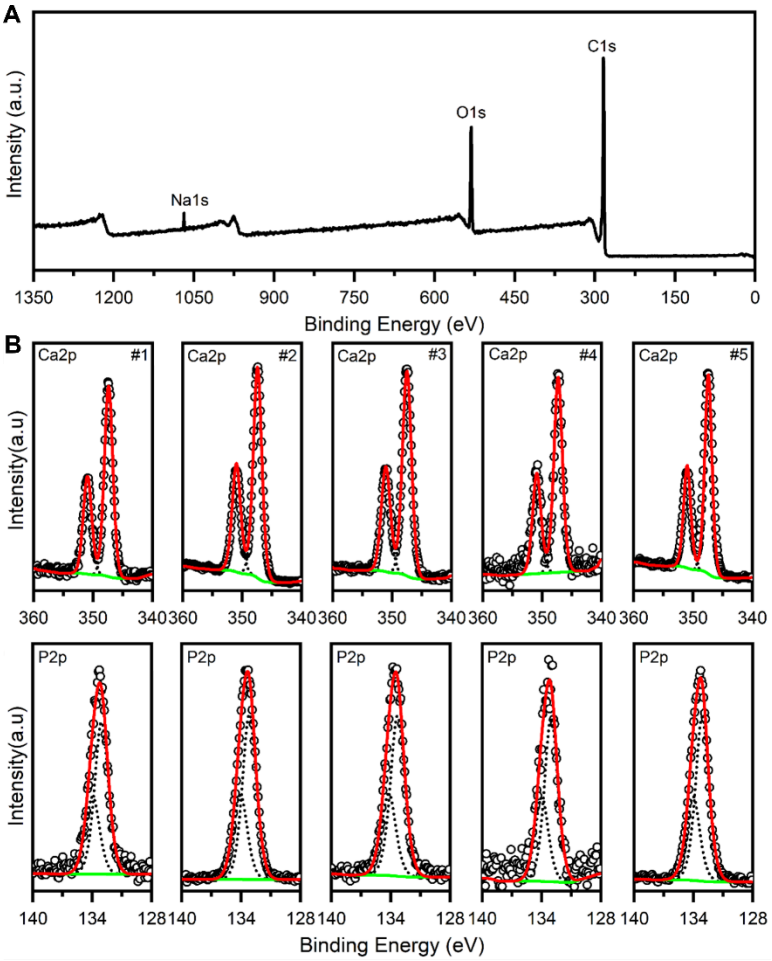

Figure S5. (A) Survey scan of location 1 on Lens 1. The primary signals are for C 1s and O 1s arising from the IOL polymer material. **(B)** High-resolution Ca 2p (top row) and P 2p (bottom row) XPS spectra of deposits on Lens 1 at five locations. Experimental data (circles), deconvoluted Gaussian peaks for Ca 2p or P 2p core-level lines (dotted lines), calculated fit (red line), and background (green line) are shown.

Table S1. Ca/P ratios of Lens 1 from high-resolution scans. The calculated standard deviation was determined in the CasaXPS program. CasaXPS uses non-linear least squares for fitting the peaks and uses a Monte Carlo approach to determine error in the area.[2]

IOL locations	Ca/P	St. Dev.
1	1.55	0.07
2	1.55	0.02
3	1.46	0.04
4	1.71	0.14
5	1.53	0.03
Average	**1.53**	**0.09**

Subsurface Evaluation of Lens 3:

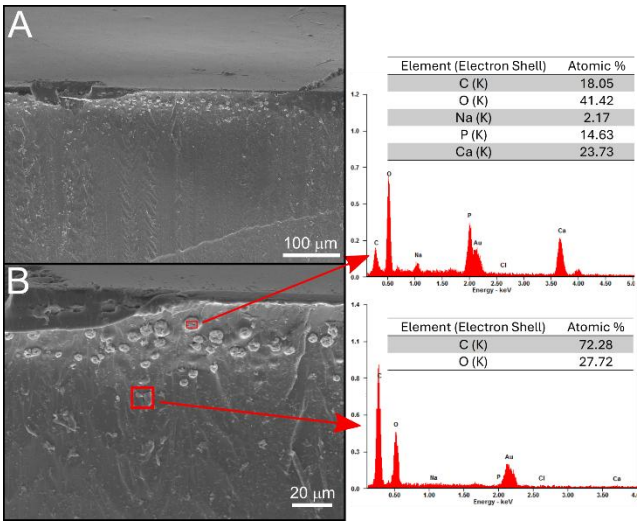

Figure S6. (A) Cross-sections of Lens 3 (200x magnification) showing crystal formation occurring inside the lens without any crystals on the surface. **(B)** Zoomed in region near the lens surface (700x) shows crystals forming inside the lens. Crystals range from 1–10 µm in diameter. No porous microchannels appear to be present between the lens surface and the crystals. EDS data confirm that crystals consisted of Ca, P, and Na (top) whereas other subsurface areas are only comprised of C and O from the lens polymer (bottom).

Images of non-calcified Lenses 6 and 7:

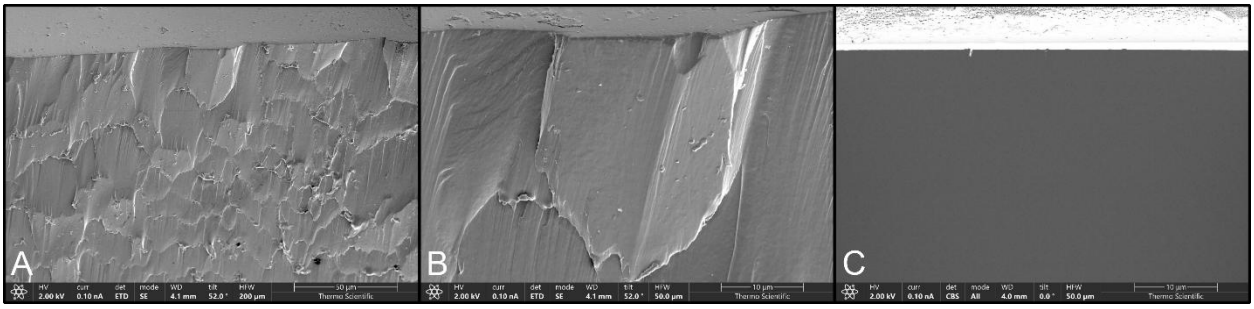

Figure S7. Cross-sectional SEM images from Lens 6 **(A)** cut with a razor blade, **(B)** higher magnification of **A**, **(C)** milled with FIB and detected with a concentric backscatter detector to provide elemental contrast. Lens 6 was explanted from a patient but does not show any crystals or porous features. FIB did not damage the lens polymer unlike the razor blade.

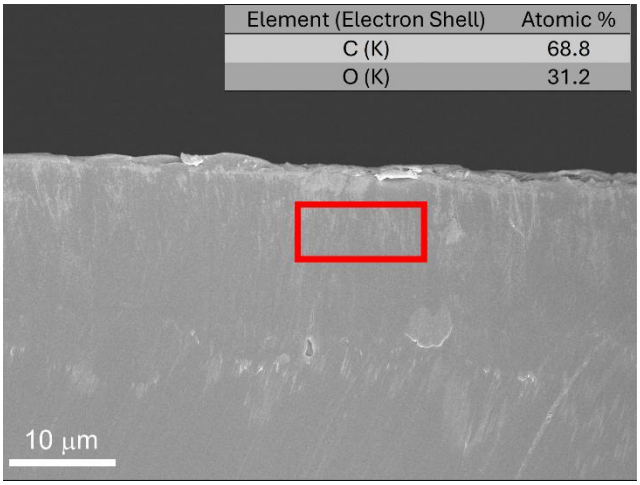

Figure S8. Cross-sectional SEM images and EDS results of Lens 7 cut with a razor blade.

Background Signal Subtraction for Powder XRD of IOLs:

XRD analyses exhibit an amorphous background signal from the oil used to mount the sample, which was removed using the Bruker program, EVA, for **Figures 4D** and **S1D, S2E, S3D, S4E**. Raw background signal from the oil is shown in **Figure S9** (red) along with oil coated on a control IOL (Lens 6; blue). To demonstrate that the single-crystal diffractometer (SCD) can effectively detect the signals at low 2θ angles, above the amorphous signal from the lens and oil, Lens 6 was lightly coated with oil and with either HAP or OCP powder. Despite the background signals from the amorphous oil and the polymeric lens material (**Figure S9,** red and blue traces, respectively), clear signals were observed for the HAP and OCP above the amorphous background signal (**Figure S9,** black and green traces, respectively). These data demonstrate the effectiveness of our SCD method to obtain powder patterns from micrograms of sample on small, curved, amorphous materials.

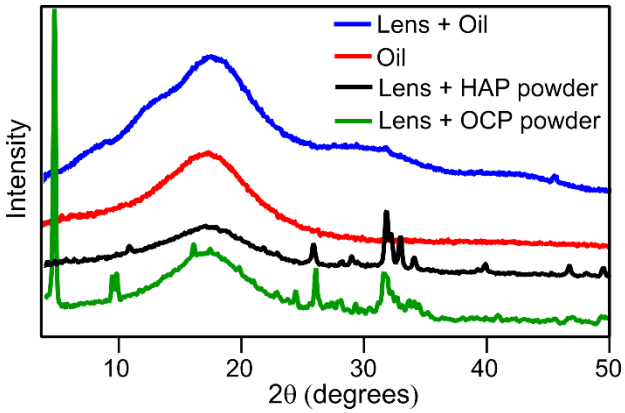

Figure S9. Powder XRD patterns of a control lens coated in mounting oil (blue) and either HAP powder (black) or OCP powder (green). The red trace depicts signal with only oil on the mount, which produces the amorphous peak at ~18°.

Raman Signals from Lens 1:

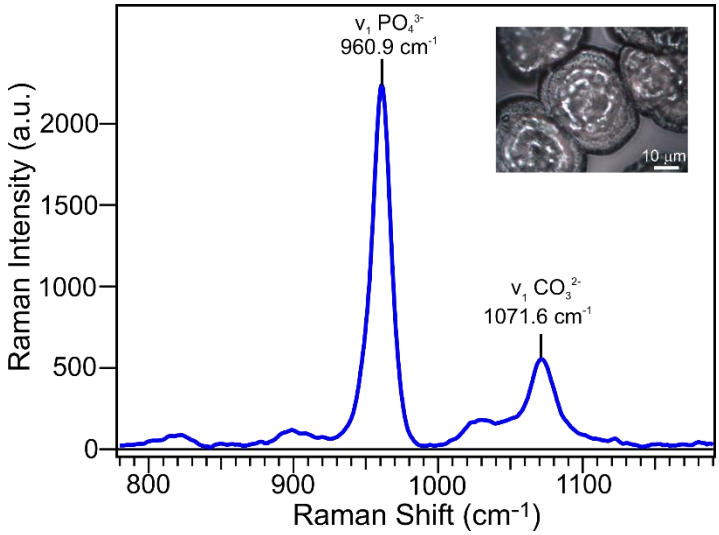

Figure S10. Raman spectrum for Lens 1 with the main peak at 960.9 cm^{-1} for the $v_1(PO_4^{3-})$ mode and a smaller peak at 1071 cm^{-1} due to $v_1(CO_3^{2-})$. The inset shows a micrograph of the crystal from the Raman confocal microscope.

Rietveld Refinement (RR) Details:

RR uses structural information from a crystalline substance (i.e. lattice parameters, atomic coordinates, etc.) and instrument peak shape profiles to derive a calculated powder pattern to compare with the experimentally measured powder pattern. A series of parameters are refined to minimize the difference between the calculated pattern and the experimental pattern using least-squares refinement. TOPAS 5 (Bruker) was used for the RR analyses herein. The crystallographic information file (CIF) for stoichiometric HAP from a single crystal dataset was used as the initial model structure to fit the powder patterns listed in **Table 2** of the manuscript.[3]

First, instrument parameters had to be established, so a Si standard reference material (Deane K. Smith, X-ray Diffraction Accessory, *a*=5.4310) was added to patient IOLs and the HAP powder during data collection using the SCD. The diffraction patterns with Si determined the zero error and the U, V, W, and X values for the modified Thompson-Cox-Hastings pseudo-Voigt (pv_TCHZ) peak-shape function. These parameters were optimized for Si and fixed for subsequent analyses of the lenses and HAP powder collected without the Si reference. Additionally, sample displacement and Lorentz-polarization factor (Lp) were fixed at zero for subsequent IOL analyses. The following variables were refined for each proposed phase to fit the experimental powder data: the unit cell parameters (*a* and *c*); Chebychev coefficients (5

coefficients); crystallite size (L); the sample scaling value, and the background peaks from the amorphous lens material (**Figure S9**) using four Pearson VII peaks (peak position, FWHM, and exponents for the composite functions). The results of the unit cell parameters using stoichiometric HAP are presented in **Table 2** in the manuscript. The results showed that unit cell parameter *a* decreased for patient IOLs compared to the NIST standard and the powder HAP samples on the SCD.

Additionally, to ensure the accuracy of the SCD results for the unit cell parameters, HAP powder was also analyzed on a standard powder diffractometer. A Bruker D8 ADVANCE was used with a 280 mm goniometer radius, Soller slits of 2.5°, fixed divergence slit of 0.2 mm, Cu K_α X-rays generated at 40 kV and 40 mA, a Lynxeye_XE_T position sensitive detector, receiving antiscatter slit was 4.988 mm, and the receiving Soller slit for axial divergence was 2.5°. Diffractograms were collected from 8 to 90° with 0.015° step size and step time of 4.0 s/step. The peak shapes were modeled using fundamental parameters with the above diffractometer information. Additionally, the variable for flat sample absorption correction was allowed to refine and the Lp was fixed to zero. The results of the lattice parameters from the RR are in **Table 2** in the manuscript. The comparison of the HAP powder collected on the powder diffractometer versus the SCD were identical, which indicates that the use of the SCD using the Thompson-Cox-Hastings pseudo-Voigt peak shape function for the RR does not affect the results. Furthermore, the lens material itself does not impact the analysis, as demonstrated by coating HAP on a control IOL.

Structural Refinement Using Rietveld Refinement:

To incorporate sodium and carbonate into the RR fit of the IOL crystals in **Figures 6A and 6B**, the crystal structure of HAP was modified. In both cases, the atomic positions from the X-ray crystal structures were fixed. When atomic positions were allowed to refine, the oxygen atoms for the phosphate and carbonate molecules moved to larger/smaller bond lengths than possible. This is likely due to disorder in the substituted structure distorting the average measured bond lengths. This disordered structure is too complex to model with the powder data collected. Thus, the Rietveld analysis was performed keeping the atom positions fixed. Only visual differences in peak intensities were reported between the two proposed models.

The two proposed chemical formulas for the IOL deposits were based on our spectroscopic data and literature precedence and used to compare the two extremes where a large Ca vacancy provided good agreement with the measured elemental ratios but produced a poor fit to the powder data and the opposite scenario where XRD results matched well but

elemental ratios did not. Visual inspection of the resulting fits and the difference plots were used for evaluating the comparisons between the two chemical formulas.

HAP $Ca_{7.5}Na_{0.7}(PO_4)_5(CO_3)_1(OH)_{0.2}$: The single-crystal structure of HAP ($Ca_{10}(PO_4)_6(OH)_2$) was used as the starting structure.[3] The atomic positions were fixed while the lattice parameters were allowed to vary, with anisotropic displacement parameters fixed at 1. The crystal structure of HAP contains two distinct sites for Na^+ to exchange with a Ca^{2+} in the structure (**Figure S11**). They are labeled as Ca(1) and Ca(2). The Ca(2) site is generally the site that undergoes Na^+ exchange as the distance to the nearest oxygen atoms are further compared to Ca(1), reducing any interactions.[4] Thus, only Na(2) (sodium that exchanges for the Ca(2)) was included in the model. This structure also incorporates the CO_3^{2-} molecule on two of the PO_4^{3-} tetrahedral faces (**Figure S12**), which has been demonstrated by other publications on synthetic cHAP powders.[5] It was assumed Na(2) occupied the Ca(2) site, leaving no vacancy while the atomic occupancies for Ca(1) contained the vacancies needed for the structure to possess 7.5 Ca atoms. This assumption was based on previous synthetic sodium B-Type HAP RR results.[4] Thus, Ca(1) and Ca(2) were fixed at 0.55 and 0.883, respectively. The atomic occupancy for Na(2) was fixed to 0.117. The atomic occupancies for P(1) was fixed at 0.8333, C(1) fixed at 0.0835, and O(3) fixed at 0.9165.

HAP $Ca_9Na_1(PO_4)_5(CO_3)_1(OH_2)$: The single-crystal structure of HAP ($Ca_{10}(PO_4)_6(OH)_2$) was used as the starting structure.[3] The atomic positions were fixed while the lattice parameters were allowed to vary, with anisotropic displacement parameters fixed at 1. This structure also incorporates the CO_3^{2-} molecule on two of the phosphate tetrahedral faces (**Figure S12**), which has been demonstrated by other publications on synthesized cHAP powders.[5] The atomic occupancies for Ca(1) was fixed at 1 while Ca(2) was fixed at 0.8333. Only Na(2) was included in the models in the Ca(2) sites (as described above).[4] The atomic occupancy for Na(2) was fixed to 0.167. The atomic occupancies for P(1) was fixed at 0.8333, C(1) fixed at 0.0835, and O(3) fixed at 0.9165.

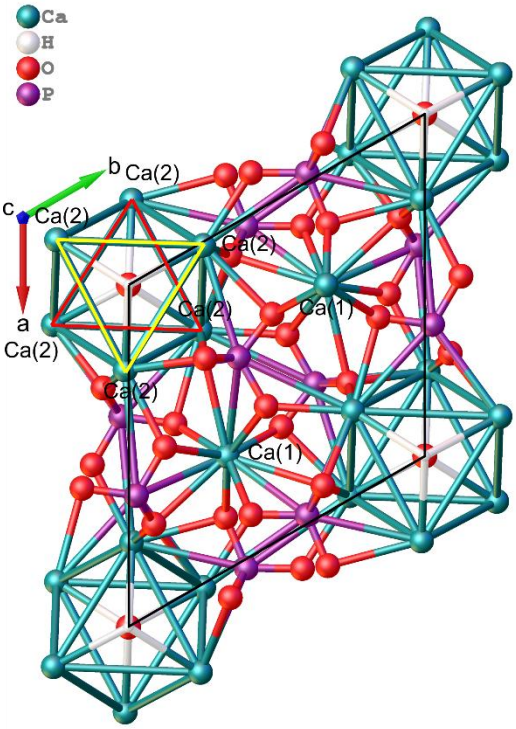

Figure S11. Structure of stoichiometric HAP. There are six crystallographically equivalent Ca(2) atoms and four crystallographically equivalent Ca(1) atoms. The sodium likely occupies the Ca(2) atomic sites for the two proposed models.

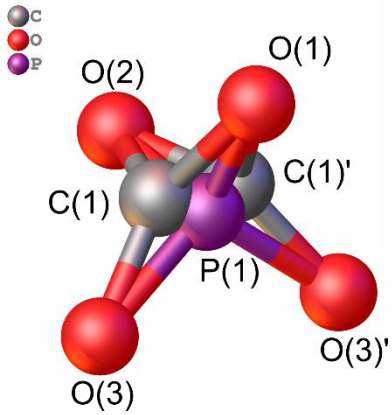

Figure S12. Image of the incorporation of carbonate ion into the same positions at the phosphate ion of HAP. The O(1)-P(1)-O(2) atoms lie on a mirror plane so O(3) and C(1) generate C(1)' and O(3)' by reflection. The carbonate ion is also disordered by this symmetry operation so they are located equally in both positions.

References

1. A. G. Shard, *J. Vac. Sci. Technol. A.*, 2020, **38**, 041201.
2. P. J. Cumpson and M. P. Seah, *Surf. Interface Anal.*, 1992, **18**, 345-360.
3. K. Sudarsanan and R. A. Young, *Acta Crystallogr. B.*, 1969, **25**, 1534-1543.
4. O. F. Yasar, W.-C. Liao, R. Mathew, Y. Yu, B. Stevensson, Y. Liu, Z. Shen and M. Edén, *J. Phys. Chem. C*, 2021, **125**, 10572-10592.
5. T. I. Ivanova, O. V. Frank-Kamenetskaya, A. B. Kol'tsov and V. L. Ugolkov, *J. Solid State Chem.*, 2001, **160**, 340-349.